# GPR-assisted evaluation of probabilistic fatigue crack growth in rib-to-deck joints in orthotropic steel decks considering mixed failure models

Heng, Junlin; Zhou, Zhixiang; Zou, Yang; Kaewunruen, Sakdirat

*DOI:*
10.1016/j.engstruct.2021.113688

# GPR-assisted evaluation of probabilistic fatigue crack growth in rib-to-deck joints in orthotropic steel decks considering mixed failure models

Junlin HENG[a, b], Zhixiang ZHOU[a,*], Yang Zou[c], Sakdirat Kaewunruen[d]

[a] Department of Civil Engineering, College of Civil and Transportation Engineering, Shenzhen University, Shenzhen 518060, China

[b] Department of Engineering Structures, School of Civil Engineering and Geosciences, Delft University of Technology, Delft 2628 CN, the Netherlands

[c] Department of Bridge Engineering, School of Civil Engineering, Chongqing Jiaotong University, Chongqing 400074, China

[d] Department of Civil Engineering, School of Engineering, University of Birmingham, Birmingham B15 2TT, the United Kingdom

**Abstract**: Rib-to-deck (RD) welded joints in orthotropic steel bridge decks demonstrates two major fatigue failure models, including the toe-to-deck (TTD) cracking and root-to-deck (RTD) cracking. Generally, the sole failure model is employed in the fatigue assessment of RD joints, which caused a hot debate on the dominant failure model. In this paper, the fatigue life of rib-to-deck has been evaluated in a probabilistic way with considering mixed failure models. A probabilistic fatigue crack growth (PFCG) model is at first established for the RD joint using fracture mechanics. In the PFCG model, two crack-like initial flaws are assumed at the weld toe and root of the RD joint. Then, the RD joint is idealised by a parallel system considering the two failure models, i.e., the failure of the joint occurs once critical size is reached in any model. Meanwhile, a typical OSD bridge is selected as the prototype to derive the vehicle-induced stress spectra in RD joints. In simulating the uncertainty in vehicle loads, a random traffic model is implemented with the multi-scale modelling via the Monte Carlo simulation (MCS). After that, the machine learning tool, gaussian process regression (GPR), is used to assist and boost the fracture analysis in the PFCG simulation. With the trained and validated GPR, the computational efficiency could be remarkably improved with the dedicated balance between accuracy, efficiency and flexibility. Based on the derived stress spectra and the GPR model, the PFCG model could be implemented using MCS. After that, the result from the PFCG simulation discussed in detail, including the fatigue failure model, fatigue reliability and life prediction, crack size evolution and remain fatigue life. In the normal case that the same initial flaw is assumed at the root and toe, the RD joint shows a slightly higher possibility of RTD cracking compared with the TTD cracking. By contrast, in the parallel case that a larger initial flaw is assumed at the weld toe due to inferior welding quality, the TTD replace the RTD as the primary failure case. However, in both cases, the secondary failure model still contributes a lot to the fatigue failure and could not be ignored. As a result, a remarkable reduction can be observed in the fatigue reliability of RD joints when considering mixed failure models. Further investigation is made on the crack size evolution during the FCG process, including the crack size and aspect ratio. After that, the remain fatigue life estimation is performed on RD joints, revealing progressive accumulation of failure probability. This research not only highlights the influence of mixed failure models on the fatigue performance of welded joints, but also provide an insight into the application of machine learning tools in solving the structural deterioration issue.

**Keywords:** Orthotropic steel deck; Rib-to-deck joint; Mixed failure models; Probabilistic fatigue crack growth; Gaussian process regression.

## 1. Introduction

### 1.1 Research problem

*Mixed failure models in RD joints*

The orthotropic steel deck (OSD) [1] is a highly integral deck system fabricated with various types of welded connections. Among all the connections, the rib-to-deck (RD) welded joint accounts for the largest proportion, e.g., 50 times the bridge length of the RD joint can be observed in a typical OSD [2]. Moreover, the RD joint is directly influenced by the cyclic vehicle loads, as shown in Fig.1. As a result, the RD joint becomes very prone to fatigue cracking after the bridge has been exploited for several decades [3], which hinders the further application of OSDs even if they illustrate superior performance and capacity over other deck systems. In the RD joint, the weld toe and weld root are two critical sites for fatigue cracking due to the notable welding residual stress and discontinuity in geometry and material [4]. Accordingly, two different patterns of fatigue failure are observed in RD joints, including the toe-to-deck (TTD) crack and the root-to-deck (RTD) crack, as depicted in Fig.1. Both the TTD crack and RTD crack are detrimental to the serviceability and durability of OSDs, which is of particular concerns in the fatigue design.

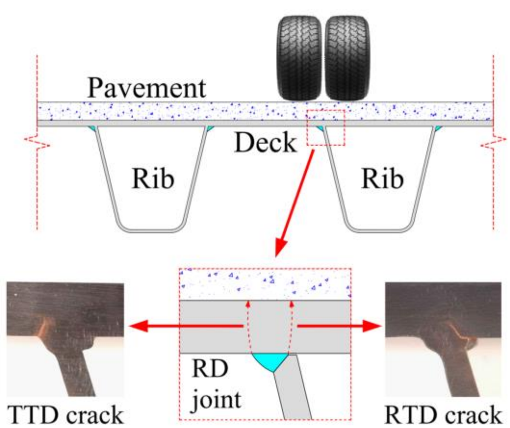

Fig. 1. Typical failure model of rib-to-deck joints

*Uncertainties in fatigue crack growth*

As generally acknowledged, the fatigue crack growth (FCG) of welded connections is affected by a list of complicated factors with notable uncertainties [5]. To this end, the FCG process in RD joints becomes highly stochastic, which incurs difficulties in fatigue assessment. Besides, the uncertainty also results in the variation in the fatigue failure pattern in the RD joint, i.e., both the TTD cracking and RTD cracking were reported in the fatigue test and field inspection of OSDs [6]. To this end, a hot issue is still open to discussion over the fatigue cracking pattern of RD joints.

1.2 State-of-the-art review

*TTD or RTD cracking*

The TTD cracking (as shown in Fig. 1) is commonly observed in the model fatigue test using the full-scale RD specimen [7], which consists of a deck plate and a closed U-ribs connected by two RD joints. Tian et al. [8] conducted the fatigue test of 7 RD specimens fabricated by partial joint penetration (PJP) welding. The TTD cracking was observed in 6 of 7 specimens, while only one shows the root-to-throat cracking. Heng et al. [9] carried out a similar fatigue test of 7 full-scale RD specimen, in which the TTD crack was found in all the specimens. The test also suggests that the fatigue crack initiates at the deck toe and then grows in both the length and thickness direction of the deck until the failure. In the further study by Heng et al. [10], 4 more specimens were tested with the special effort to monitor the crack growth. Besides the same observation of the TTD cracking, the monitoring result suggests the semi-elliptical crack shape during the propagation. Similar tests were performed on RD specimens by Cheng et al. [11], Nagy et al.[12] and Li et al. [13], which also suggests a dominance of TTD cracking. It is worth noting that a systematic fatigue test panel of RD joints was performed by Ocel et al. [14], with a total of 185 RD specimens. Except for the 30 runouts, the remain 155 specimens shows a remarkably high proportion of TTD cracking, i.e., 125 specimens with TTD cracking (about 81%). Among the 30 specimens without TTD, 16 specimens were fabricated with a large root gap deliberately, leading to the RTD cracking.

As aforementioned, the RTD cracking is another primary failure model of RD joint, especially when using the partial joint specimen [15]. Ya et al. [16] employed the rotational vibrator to test the partial joint specimen, consisting of a deck plate and a truncated rib wall. The RTD cracking was observed in all the 20 specimens with notable length, while only one mild TTD crack (95 mm-long) was found accompanied by a larger RTD crack (250 mm-long). Lv and Li [17] performed a similar fatigue test using the hydraulic loading machine, which also suggests the RTD cracking in all the 9 specimens. In addition, Fu et al. [18] tested 40 similar partial joint specimens, with the RTD cracking observed in all the specimens.

Besides the pure TTD or RTD cracking, the two failure models were also simultaneously observed in the full-scale OSD specimens. Sim et al. [19] tested 6 full-scale OSD specimens of 10000 mm-long and 3000 mm-wide, which consists of 4 U-ribs and 3 floor beams. Three types of welding were used, including the 80% PJP, weld melt through (WMT), and the one alternating between 80% PJP and WMT every 1000 mm. A total of 7 cracks were observed in the 3 cracked specimens, 6 of which were TTD cracking. The only RTD crack initiated from the transition between the 80% PJP and WMT. According to the result, the RD is prone to TTD cracking when the penetration rate is properly controlled. Kainuma et al. [20] carried out the fatigue test on 12 full-scale OSD specimens of 2000 mm-long and 1400 mm-wide. Overall, the 9 cracked specimens shown a dominance of RTD cracking, i.e., 6 with the RTD and 3 with the TTD.

*Preliminary consideration of mixed failure models*

As discussed above, the fatigue performance of RD joints is influenced by the mixed failure models, including the TTD cracking and RTD cracking. Conner et al. [2] suggested that the RTD cracking leads to a fatigue resistance poorer than the TTD cracking. However, the RTD cracking could be effectively prevented by the proper penetration rate (i.e., between 70% and 95% with a target of 80%) and tight fit-up gap (i.e., <0.5 mm) between the deck and U-rib. To this end, more attention and effort should be paid to the TTD cracking when the welding is implemented with reasonable configuration and procedures. Wang et al. [21] investigated the FCG behaviour of RD joint using the extended finite element method (XFEM). Two initial flaws in the same size were assumed at the deck toe and root, and the numerical result shows the comparable behaviour of the TTD and RTD cracking models. Li et al. [22] proposed the concept of governing failure model, i.e., the fatigue failure of the RD joint is only governed by the failure model with the poorest fatigue performance. Based on this notion, the equivalent structural stress is solved under various failure models and compared to determine the governing failure model and the corresponding fatigue life. Luo et al. [23] proposed a similar method using the concept of governing fatigue model, in which the strain energy density is used as the evaluation indicator instead of the stress.

*Advance in fatigue assessment*

In most of the code of practices[24][25][26], the fatigue assessment of the welded connection is made by checking the solved stress range and the number of cycles against the stress-life (S-N) curve, which is derived from the sufficient fatigue test data at the detail- or structural-level. The above S-N approach is simplified and practical but lacks transferability between different welded connections [27].

Alternatively, the fracture mechanics [28] is employed to simulate the FCG in the welded connections, which can assess different details using the material test data only [29].

The FCG process involves prominent uncertainties, including the aleatory uncertainty in its nature and the epistemic uncertainty in modelling the issue [30]. As a solution, the deterministic fatigue assessment could be conducted based on the statistics of model parameters. For instance, the design S-N curve is usually established under the survival rate of 97.7%, i.e., the mean minus two times standard deviation [31]. Meanwhile, the vehicle effect is often represented by a standard fatigue truck, which is derived from the field survey and statistics [32]. The above statistics-based approach may be conservative but cannot fully reflect the random nature of fatigue [33]. Alternatively, the direct probabilistic approach is used, including the stress-based probabilistic stress-life (PSN) approach [34][35] and fracture mechanics-based probabilistic fatigue crack growth (PFCG) method [36][37]. The PSN approach modelled the fatigue strength and vehicle configuration as random variables [38], and the result is present in the form of the probabilistic distribution or reliability index [39].

The PFCG method is much more complicated than the PSN but can provide an in-depth insight into the hidden mechanism of fatigue cracking. Maljaar and Vrouwenvelder [40] established a PFCG model of rib-to-floor beam joint using the semi-elliptical crack model with 2 degree-of-freedoms (DOFs), and the model is implemented with the analytical solution of SIFs. Heng et al. [10] proposed a similar PFCG model to derive PSN curve of RD joints considering the TTD cracking only. Likewise, Maljaar et al. [41] used the PFCG model to derive the PSN of RD joints respecting the RTD cracking. Wang [42] carried out the PFCG analysis to investigate the macro-crack initiation life (MCIL) of RD joints, which is the pre-detectable life of the crack when its depth is less than 0.5 mm. A list of 2D XFEM-based deterministic analysis was carried out to solve the SIFs for the crack sizing from 0.1 to 0.5 mm. Then, the MCIL was solved through Monte Carlo simulations (MCS) with the linear interpolation of the solved SIFs.

### 1.3 Existing research gaps

As discussed above, the RD joint is prone to mixed failure models, including the TTD and RTD cracking. The issue caused special concerns and was addressed in several pioneered works. However, the reviewed studies mainly focused on the deterministic comparison of fatigue performance under different failure models. As a result, the fatigue behaviour is solely determined after the failure model with the poorest performance, i.e., the governing model. Obviously, the non-governing failure model still has the possibility to replace the governing model and cause failure due to the prominent uncertainty. To this end, a probabilistic investigation is urgently required on the FCG behaviour of RD joints by considering the effect of mixed models.

Meanwhile, the state-of-the-art PFCG study generally employed the analytical solution or interpolation of deterministic FE results. Although the high solution cost in the PFCG simulation can be mitigated in this way, the flexibility and accuracy of FE-based fracture analysis are not fully utilised. To this end, a novel approach is to be established in order to fully incorporate the FE simulation into the PFCG analysis and to achieve the balance between accuracy, efficiency, and flexibility.

### 1.4 Aim and structure of the paper

This study aims at the probabilistic evaluation of fatigue crack growth in rib-to-deck (RD) joints of orthotropic steel decks (OSDs), with the consideration of mixed failure models. The paper is organised as the followings: in Part 2, a probabilistic fatigue crack growth (PFCG) model is established for the RD joint, assuming the initial flaw at both the weld toe and root; in Part 3, a measurement-based random traffic model is employed to derive the vehicle-induced stress spectra at the RD joint in a selected prototype bridge; in Part 4, a gaussian process regression (GPR) model is trained to surrogate the finite element (FE)-based fracture analysis, through which the solution efficiency is notably improved with satisfying accuracy; in Part 5, the result from the above studies is discussed in detail, including the fatigue failure model, fatigue reliability and life prediction, crack size evolution, and remain fatigue life; in Part 6, the major conclusions are drawn based on the above investigation. The research not only highlights the influence of mixed failure models on the fatigue performance of RD joints in OSDs, but also provides an insight into the application of machine learning tools in solving the structural deterioration issue.

## 2. Probabilistic fatigue crack growth model

### 2.1 Fatigue crack growth model

According to the above review and discussion, the crack model of RD joints is assumed with dual crack-like initial flaws at the weld toe and root, as shown Fig. 2. During the crack growth, the two cracks are assumed to stay in the perfect semi-elliptical shape with the aspect ratio varied with cycles. Thus, the crack could be idealised by a two-DOF system, including the crack depth denoted as '*a*' and the half-length denoted as '*c*'. As depicted in Fig. 2, the notation of DOFs is followed by a subscript 'tc' or 'rc', which respectively stands for the toe crack and root crack.

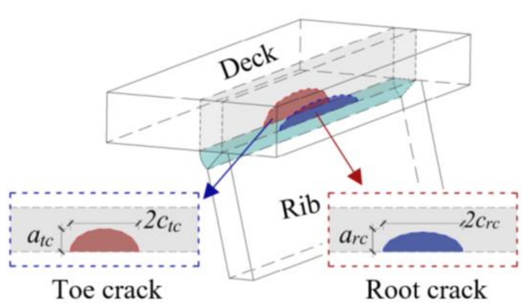


Fig. 2. Crack model of the RD joint

In simulating the FCG process, the Paris model [28] is employed to predict the increase in crack sizes with cycles, as shown in Equation 1.

$$\frac{da}{dN} = C \cdot \left(\Delta K_a(N)\right)^m, \qquad \frac{dc}{dN} = C \cdot \left(\Delta K_c(N)\right)^m \tag{1}$$

where $a$ and $c$ represent the crack depth and half-length, respectively; $N$ is the number of loading cycles; $C$ and $m$ are the crack growth rate and power index, respectively; $\Delta K_a$ and $\Delta K_c$ are the range of SIFs at the crack tip and edge, which is varied with $N$.

Based on Equation 1, the crack size at an arbitrary time $t$ can be estimated with applied loading cycles through integration, as shown in Equation 2.

$$a_t = \int_0^{N_t} \left(C \cdot \left(\Delta K_a(N)\right)^m\right) dN \tag{2a}$$

$$c_t = \int_0^{N_t} \left(C \cdot \left(\Delta K_c(N)\right)^m\right) dN \tag{2b}$$

where $a_t$ and $c_t$ are the crack depth and half-length; $N_t$ is the number of loading cycles at time $t$.

Since the explicit solution of SIFs is unavailable in most cases, Equation 2 is usually approximated by a series of fracture analysis at discrete time points, in which the crack size is gradually increasing step-by-step [43]. For enough accuracy, the increment in crack size should be limited to a reasonable value, e.g., 1% of the current crack size.

### 2.2 Probabilistic modelling of fracture parameters

Probabilistic modelling is carried out on the parameters in the proposed FCG model to consider the uncertainty in the initial flaw size and crack growth rule, as shown in Fig. 3. The initial flaw size is modelled by the flaw depth and the aspect ratio, through which the correlation between the depth and half-length of the flaw is implicitly simulated [44], as shown in Figs. 3a and b. In terms of the Paris law, the crack growth rate is modelled as a random variable, and the power index is set as a deterministic value of 3.0 as suggested by [31]. The distribution of the crack growth rate is reproduced via the mean and design value in [45], as shown in Fig. 3c.

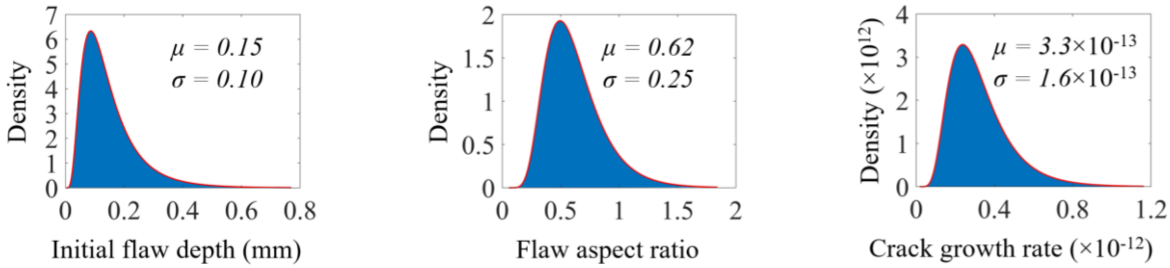


(a) (b) (c)

Fig. 3. Distribution of variables in the PFCG model: (a) Initial flaw depth [44]; (b) Aspect ratio of the initial flaw [44]; (c) Crack growth rate [45].

The critical crack size is introduced to identify the final state of the single cracking model, i.e., failure occurs once the critical size is achieved in either crack depth or length direction. In the case of crack depth, the critical size $a_f$ is set as the thickness of the deck plate. In terms of the critical half-length, a notably larger value of $c_f = 200\,mm$ is assumed, above which the safety and serviceability of OSDs would be seriously impacted [4]. The weld toe is usually completed with a welding quality inferior to that of the weld root due to the sudden arc blow-out and spatter [46], variation in the flank angle [47] and potential under-cut [48] at the toe. To this end, two cases are considered in this study: (1) Case I - the distribution of initial flaw depth and aspect ratio is the same at the root and toe; (2) Case II - the mean and standard deviation of initial flaw depth at the toe are two times the values at the root while the aspect ratio is the same.

### 2.3 Limit state function and reliability block diagram

As aforementioned, this study marks the failure of the sole cracking model by the achievement of the critical crack size in either crack depth or length. Thus, the limit state function (LSF) of a sole cracking model (i.e., TTD or RTD) can be written as Equation 3.

$$G(\dot{X}_i, t) = (a_i(t) - a_f) \cup (c_i(t) - c_f), \qquad \forall i = tc \text{ or } rc \#(3)$$

where $\dot{X}_i$ is the state vector of the *ith* cracking model.

Accordingly, the probability of failure (PF) of a sole cracking model can be derived as Equation 4.

$$P_{f,i} = P[G(\dot{X}_i, t) \le 0] = 1 - (1 - P_{f,a_i}) \cdot (1 - P_{f,c_i}), \qquad \forall i = tc \text{ or } rc \#(4)$$

where $P_{f,i}$ is the PF of the *ith* cracking model; $P_{f,a_i}$ and $P_{f,c_i}$ stand for the achievement of the critical crack size at the depth and length, respectively.

Meanwhile, the failure of the RD joint is assumed once any of the two cracking models occur. To this end, the failure of the RD joint could be idealised as a two-level hierarchical series system, as shown by the reliability block diagram (RBD) in Fig. 4.

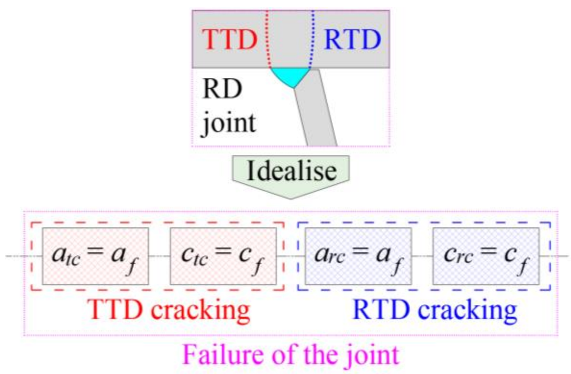


Fig. 4. System-level RBD of the RD joint

Accordingly, the system-level PF of the RD joint can be predicted using Equation 5.

$$P_{f,RD} = 1 - \left((1 - P_{f,a_{tc}}) \cdot (1 - P_{f,c_{tc}})\right) \cdot \left((1 - P_{f,a_{rc}}) \cdot (1 - P_{f,c_{tc}})\right) \#(5)$$

where $P_{f,RD}$ is the system-level PF of the RD joint; $P_{f,a_{tc}}$ and $P_{f,c_{tc}}$ are respectively the probability of the achievement of the critical size in depth and length under the TTD cracking; $P_{f,a_{rc}}$ and $P_{f,c_{tc}}$ respectively standard for the achievement of the critical size in depth and length under the RTD cracking.

The MCS is then employed to solve Equation 4 via sampling, as shown in Equation 6.

$$P_{f,RD} = \frac{\sum_{i=1}^{n_{MCS}} I\left[\left(a_{tc} \geq a_f \cup c_t \geq c_f\right) \cup \left(a_{rc} \geq a_f \cup c_r \geq c_f\right)\right]_i}{n_{MCS}} \#(6)$$

Where $n_{MCS}$ is the sample size of MCS; $I[\quad]_i$ is the true-or-false indicator by the *ith* sample.

# 3. Random traffic-based derivation of stress spectra

## 3.1 Selected prototype bridge

A typical OSD bridge in Chengdu, China, is selected as the prototype to derive the vehicle-induced stress spectra in RD joints, as shown in Fig. 5. The OSD is 12500 mm-wide, carrying three lanes with different functions. Since the fatigue-critical lorries are likely to run in the slow lane, the RD joint close to the left footprint of the centrally loaded vehicle is chosen as the joint of interest.

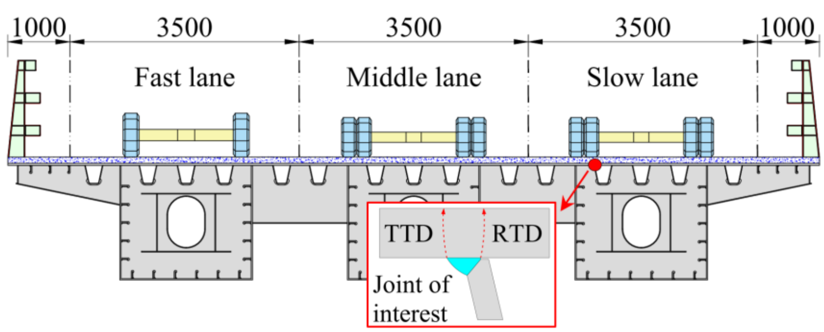


Fig. 5. Selected prototype bridge and the RD joint of interest.

## 3.2 Random traffic model

The random traffic model proposed in [49] is applied to incorporate the uncertainty in vehicle loads, as shown in Fig. 6. Overall, the vehicles have been grouped into six types with different occupancy rate in the slow lane, according to the configuration and axle weight. It is worth stating that the model excludes lightweight passenger cars because of their little contribution to fatigue damage [50]. Two kinds of axles are assumed for each vehicle type, including the steering axle marked in blue and the rear axle marked in red. Accordingly, two types of footprints are assumed, i.e., 300×200 mm (width and length) for the steering axle with single-tire and 600×200 mm for the rear axle with dual-tire.

Apart from the vehicle configuration, the axle weight of each vehicle type is also modelled as random variables. As per the feature of the axle weight, the Gaussian mixed model (GMM) is employed to fit the distribution, which could have multiple peaks. Fig. 7 shows the probability density of the weight of the 3rd axle in the type V5 vehicle, and the details about other axles can be found in [39].

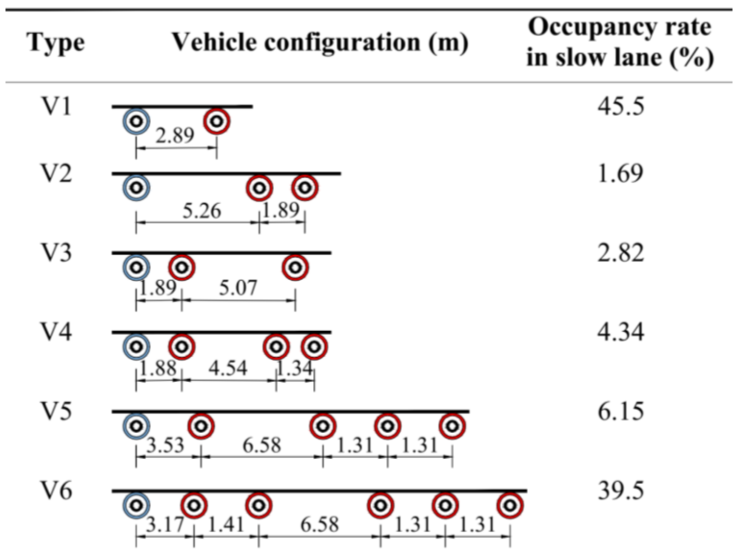


Fig. 6. The vehicle types and occupancy rate of the used random traffic model [49]

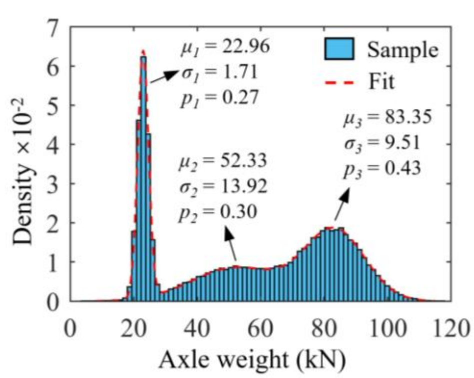


Fig. 7. Weight distribution of the 3rd axle in the type V5 vehicle

Meanwhile, the lateral distribution of the vehicle centre is considered according to EC1 [32], as shown in Fig. 8. For the convenience of numerical implementation, the original discrete distribution is fitted into the continuous Gaussian distribution. Based on the above model, the vehicles are generated through conditional sampling due to the interdependence among the variables in the random traffic model, as shown in Fig. 9.

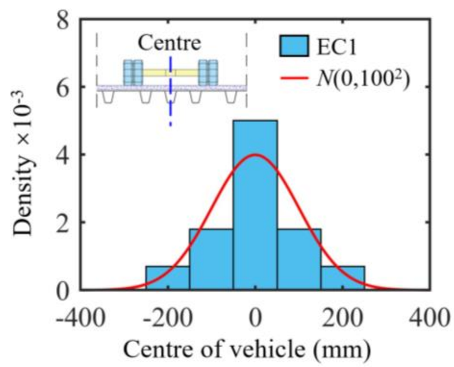


Fig. 8 Lateral distribution of vehicle centre.

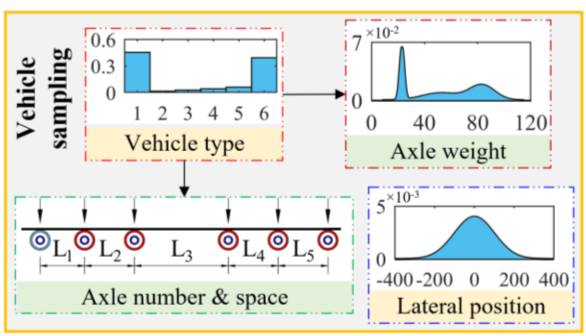


Fig. 9. Conditional sampling of vehicles

The vehicle type and lateral position are at first sampled. Then, the sample size of each vehicle type is determined after its proportion and the total sample size of MCS. Conditioned on the vehicle type, sampling is made for the number of axles, axle space, and axle weight. The number of axles and axle space are two deterministic values directly associated with the vehicle type, as shown in Fig. 6. Meanwhile, the axle weight is sampled using the edge distribution conditioned on the vehicle type, as shown in Equation 7.

$$P(W_i) = \sum_{j=1}^{6} P(V_j) P(W_i|V_j) \#(7)$$

Where $W_i$ is the weight of the *ith* axle; $V_j$ stands the *jth* vehicle type.

The traffic volume is described by the average daily traffic (ADT) with the Gaussian distribution, as shown in Fig. 10. The measurement in [49] is used to calculate the mean value of the ADT, while its standard deviation is determined after the COV of 0.2 reproduced from the data in [50].

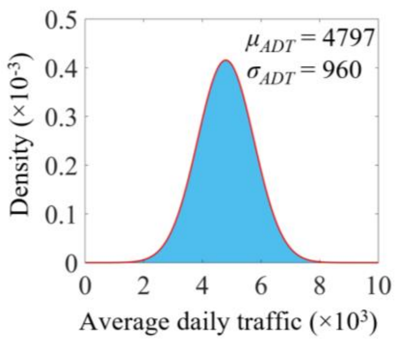


Fig. 10. Distribution of the ADT

3.3 Influence surface-based derivation of stress spectra

A multi-scale FE model of the selected bridge is established [51] to derive the vehicle-induced stress spectra, as shown in Fig. 11. For the balance between accuracy and efficiency, the FE model is modelled by three parts with different meshing strategies, including the global model of the bridge, the sub-model of the segment under investigation, and the highly refined model of the interested RD joint.

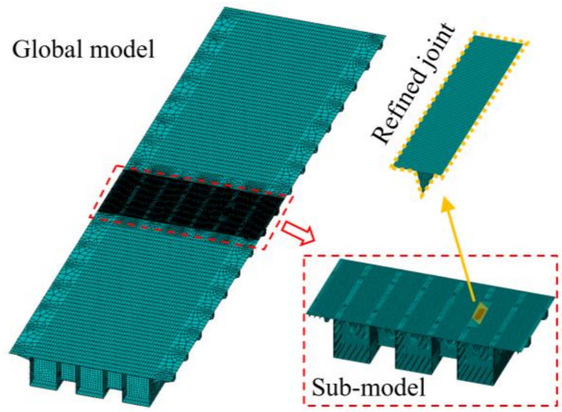


Fig. 11. Multi-scale FE model of steel bridge

The global model is meshed with a relatively coarse element size (i.e., 20 mm-wide and 50 mm-long) since it is mainly used to transfer the boundary condition from the global model to the sub-model. Then, the sub-model is discretised using a finer element size of 10×10 mm. The global model and sub-model are meshed separately and then coordinated via the multi-point constraint (MPC) algorithm [52]. Meanwhile, the refined model of the interested RD joint is directly embedded into the sub-model by the sharing nodes on the interface. To this end, the adaptive meshing is employed to generate a smooth transition of element size from 10×10 mm to 2×2 mm at the core region where the stress to be extracted. The influence surface method [39] is exploited to boost the FE model-based derivation of the stress spectra using the random traffic model. Figs. 12 shows the influence surface solved for the dual-tire of 60 kN.

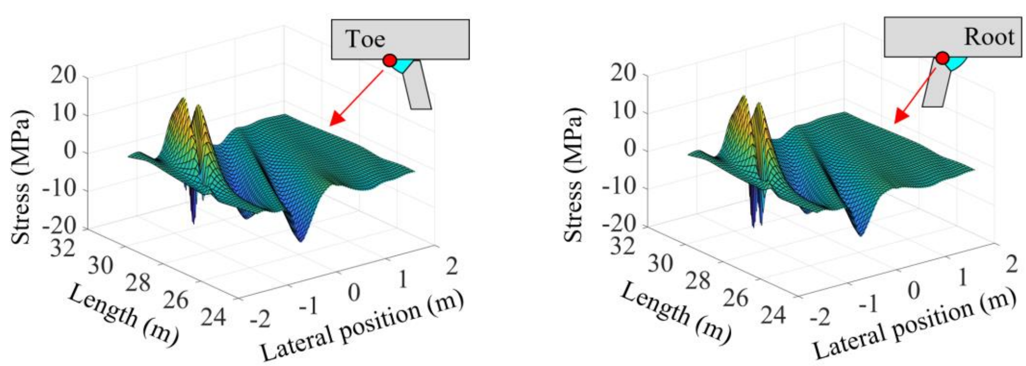


(a) (b)

Fig. 12. Influence surface of stress under the dual tire of 60 kN: (a) Weld toe; (b) Weld root.

Based on the influence surface, the stress history of a sampled vehicle could be easily derived by the linear operation. For the illustration purpose, a standard V6 truck is applied to derive the stress history at the weld toe and root, as shown in Fig. 13.

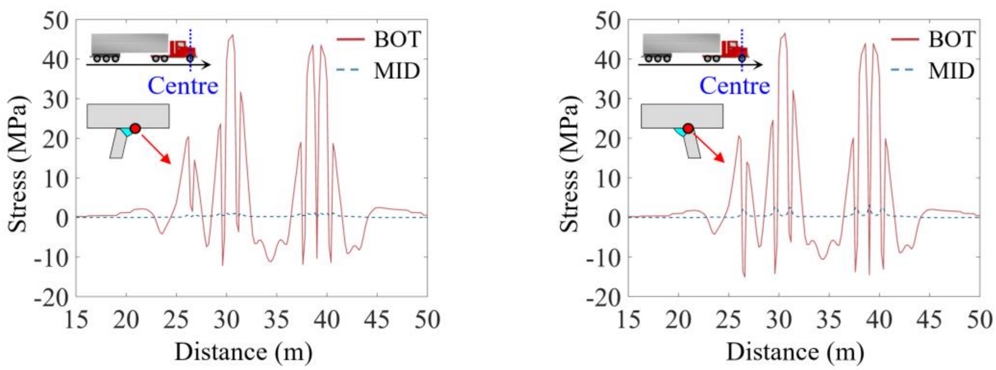


(a) (b)

Fig. 13. Stress history solved with the standard V6 truck: (a) Weld toe; (b) Weld root.

The axle weight of the standard truck is set as the upper quantile of 97.7%, and the truck is assumed to pass through the centre of the slow lane. Obviously, one stress range is generated by each axle. Besides, it is interesting that the stress at the middle surface is almost ignorable compared with the stress at the bottom surface. Thus, only the bending stress is considered in the SIF calculation in the following section.

Based on the above method, a comprehensive database of the stress history is derived through a total of $10^7$ MCS. After that, the rain-flow approach [53] is used to transform the stress history into a series of stress ranges and the corresponding number of cycles. Recalling the Paris law in Equation 1, since the same crack size is assumed in a single solution step, the above stress ranges could be converted into one equivalent stress range, as illustrated in Equation 8.

$$\Delta\sigma_e = \sqrt[m]{\sum_{i=1}^{n_{sr}} N_i \cdot {\sigma_i}^m} \#(8)$$

where $\Delta\sigma_e$ is the equivalent stress range; $n_{sr}$ is the number of stress ranges; $\sigma_i$ and $N_i$ are the *ith* stress range and the corresponding number of cycles.

Then, the database of equivalent stress range is established and fitted via the GMM model, as shown in Fig. 14. The distribution of the equivalent stress range shows two crests with similar proportions (i.e., 45% vs 55%), including a narrow peak in the lower region and a flat one centred on the upper region.

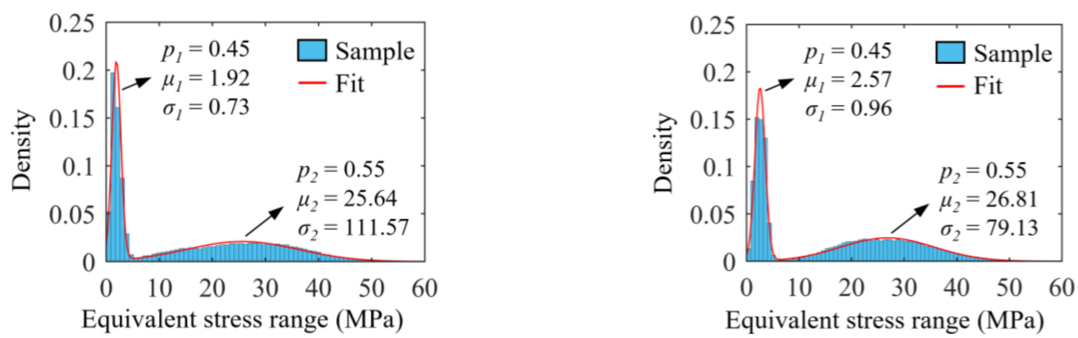


(a) (b)

Fig. 14. Stress spectra derived by random traffic model: (a) Weld toe; (b) Weld root.

The lightweight steering axle is deduced as the major cause for the crest in the lower region, for which the density enriches to form a narrow peak. On the contrary, the crest in the upper region is induced by the rear axle, of which the diversity in weight leads to the flatness of the crest.

## 4. Gaussian process regression-assisted solution of SIFs

As aforementioned, the extremely high computational cost hinders the application of FE-based PFCG simulation. This study tries to find an alternative solution by hiring the machine learning tool, Gaussian process regression (GPR) [54], to boost the FE-based PFCG analysis. The most prominent feature of the GPR is the exploitation of the covariance between the various data points, as shown in Equation 9.

$$g(\dot{x}) = \xi(\dot{x})^T\dot{\theta} + f(\dot{x})\#(9a)$$
$$f(\dot{x}) \sim GP\big(0, r(\dot{x}, \dot{x}')\big)\#(9b)$$

where $g(\dot{x})$ is the total response on the $n_d \times 1$ input vector $\dot{x}$; $\dot{\theta}$ is a $n_p \times 1$ vector defining the parameters in the basis function; $\xi(\dot{x})$ stands for the explicit function to transform $\dot{x}$ from $\mathbb{R}^{n_d}$ to $\mathbb{R}^{n_p}$ space; $f(\dot{x})$ is the lament function which follows the zero-mean Gaussian process; $r(\dot{x}, \dot{x}')$ is the kernel function simulating the covariance.

In the GPR, the influence of each train data point increase as the point of prediction moves towards it due to the application of the kernel function. As a result, the GPR demonstrates a good accuracy when interpolating with well-distributed train data [55]. In preparing the train data for the GPR, a local FE model of the RD joint is established using ANSYS [51], as shown in Fig. 15. The multi-scale modelling strategy is also applied, for which the local model and the highly refined crack body are separately meshed. Then, the crack body is connected with the local model via the surface-to-surface contact [52]. By employing the local FE model, a list of train data could be generated for the SIF with different crack size under the unit bending stress, as shown by the small blue maker in Figs. 16 and 17.

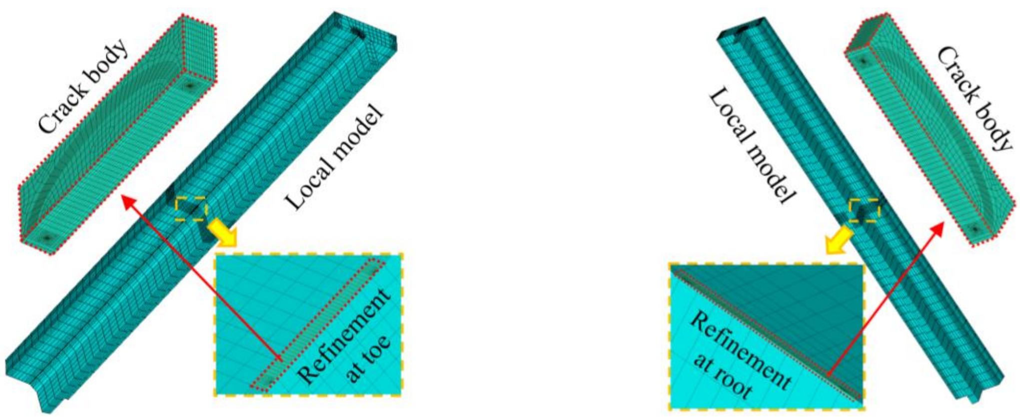


(a) (b)

Fig. 15. Local FE model for fracture analysis: (a) Weld toe; (b) Weld root.

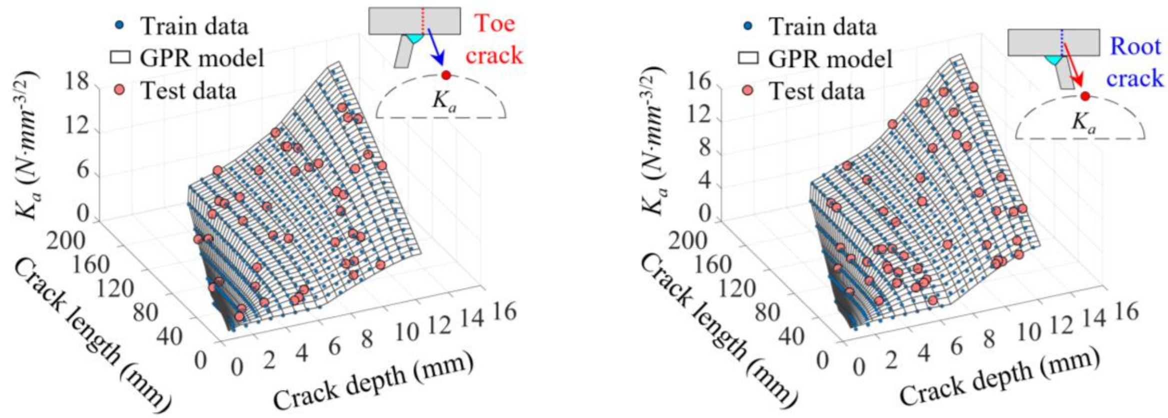


(a) (b)

Fig. 16. GPR training and validation of SIF at the crack tip: (a) Weld toe; (b) Weld root.

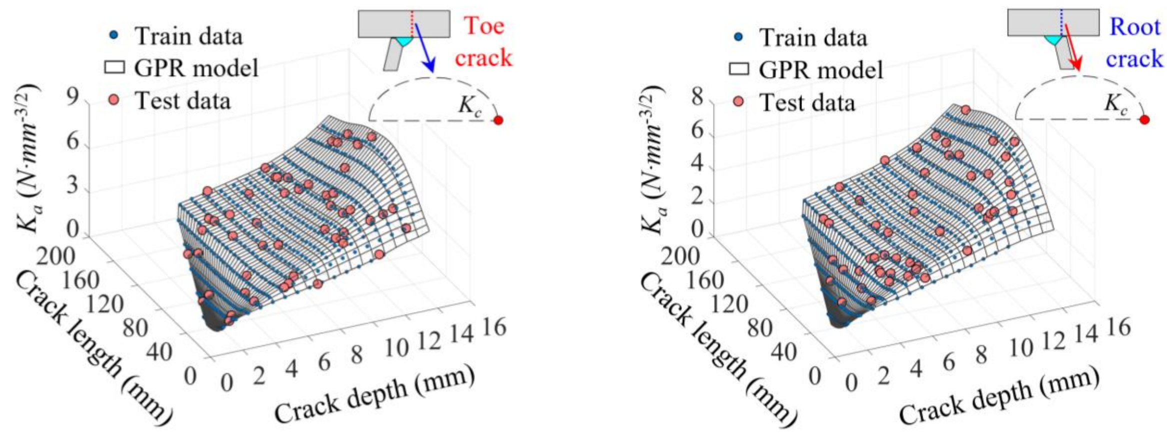


(a) (b)

Fig. 17. GPR training and validation of SIF at the crack edge: (a) Weld toe; (b) Weld root.

The GPR model is trained using the solved data, as shown by the grey grid in Figs. 16 and 17. For the validation purpose, a series of inputs are randomly sampled and solved via the local FE model, as shown by the big red marker in Figs. 16 and 17. The result suggests an excellent agreement between the FE solution and the GPR prediction, indicating the accuracy and feasibility of the trained GPR model.

The trained and validated GPR model is used to surrogate the FE-based fracture analysis in the SIFs calculation, as shown in Fig. 18. Compared with the direct solution using the FE model, the computation cost can be greatly reduced through the GPR-assisted simulation. For instance, a total of 20.8 hours may be spent to generate a single sample by implementing the FE-based fracture analysis with a 10-core (Intel i9-10900K) workstation [56]. Exactly, the efficiency is much higher than the model fatigue test, which usually costs one or two weeks to complete only one specimen. However, the efficiency is still far behind the need for extensive solution efforts imposed by the PFCG analysis.

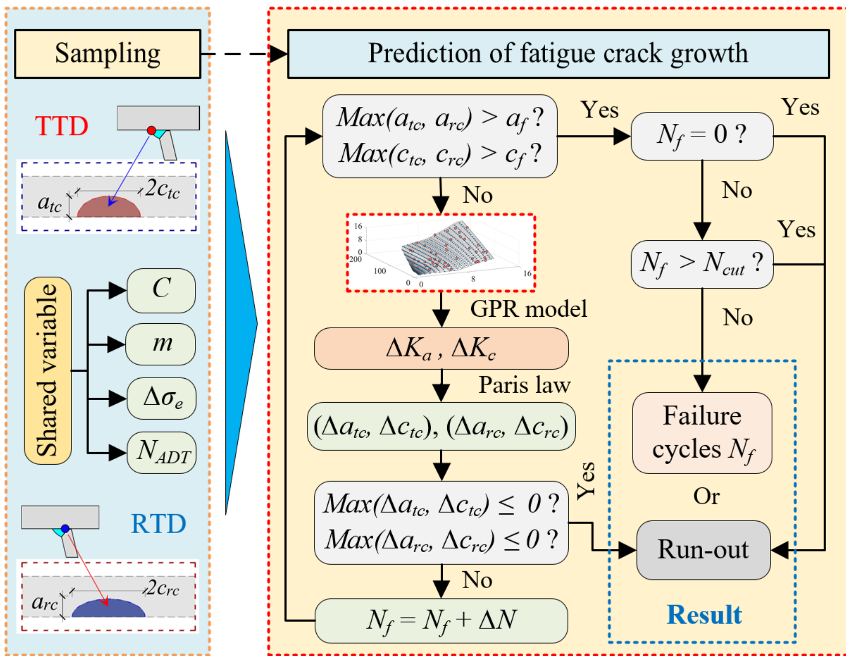


Fig. 18. Flow chart of GPR-assisted solution using the PFCG model.

Alternatively, with the same hardware, the solution time for a single data point using the GPR-assisted approach can be less than 40 seconds, i.e., more than 1800 times improvement in the computational efficiency. As a result, the flexibility and accuracy of FE-based fracture analysis could be fully incorporated into the PFCG simulation.

# 5. Result and discussion

## 5.1 Fatigue failure model

The FCG history of the RD joint could be solved by implementing the PFCG model with the

GPR-assisted approach. Figs. 19 a and b show the FCG process of two typical failure models solved under the case I and case II (see Section 2.2), respectively. For better illustration, the mean value of variables is utilised in the calculation. In the case I, the initial flaw size is assumed the same at the weld root and toe. Compared with the toe crack, the root crack shows a slightly higher growth rate and causes the failure of the joint. In the case II, the toe crack replaces the root crack as the failure case. In addition, the final critical crack size of the toe crack is notably larger than that of the root crack in the case II. To sum, the RD joint is prone to the root cracking when the same initial flaw is assumed. However, as a larger initial flaw is assumed at the weld toe in the case II, the toe crack becomes the critical case of the failure.

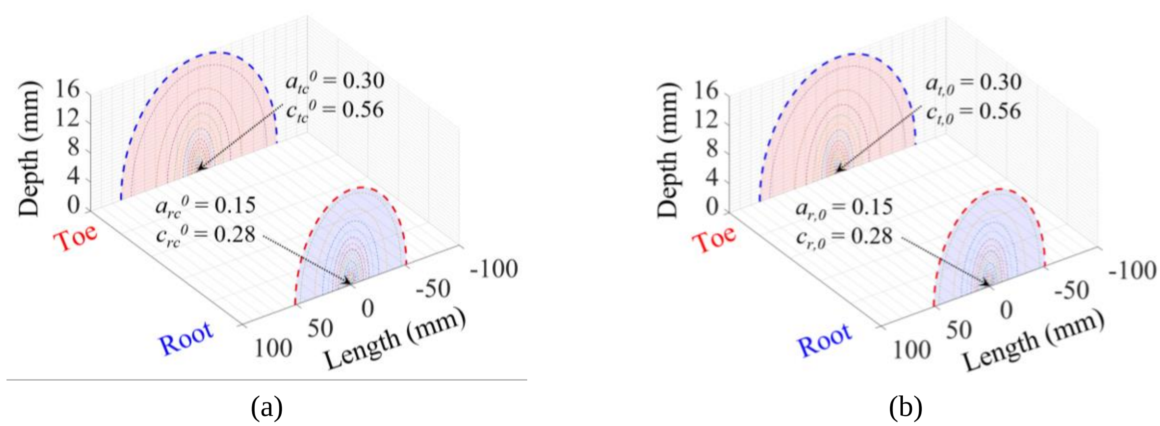


Fig. 19. FCG process of two typical fatigue failure models: (a) Case I; (b) Case II.

Apart from the above two failure models, the RD joint also illustrates a third failure model, in which both the toe and root cracks reach the critical size at the same time. However, this both-cracking failure is a coincident event rarely that happens in a sense of statistics. A total of $10^6$ MCS are performed to investigate the proportion of the three failure models, as shown in Fig. 20.

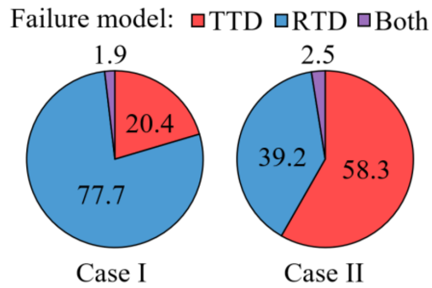


Fig. 20. Proportion of different failure patterns.

In both the cases I and II, the both-cracking failure shows a proportion well below 2.5%, which could be regarded as an event of small probability [57]. In the case I, the probability of the RTD cracking is about 281% higher than that of the TTD cracking, i.e., 77.7% vs 20.4%. In the case II, the RD shows an increased tendency of the TTD cracking about 49% higher than that in the cracking. Generally, both the TTD cracking and RTD cracking contributes to the fatigue failure notably. However, this effect would be overlooked if only the governing failure model is employed to assess the fatigue performance. Meanwhile, from a statistical point of view, the dominance of failure models depends on the initial flaw size, which represents the welding quality.

## 5.2 Fatigue reliability and life prediction

Further investigation is made on the fatigue reliability and life prediction of the interested RD joint (see Fig. 5). For better comparison, the reliability is also estimated using the PSN approach proposed in [39], with the same fatigue strength assumed for the TTD cracking and RTD cracking. A total of $10^7$ MCS are conducted for the service life from 20 to 120 years, as shown by the time-variant reliability curve in Fig. 21. Since the OSD is a highly redundant system, its fatigue cracking is more likely an issue of serviceability [58]. According to JCSS [59], three reliability levels (i.e., 1.3, 1.7 and 2.3) are introduced for the comparison and life prediction, which are denoted as the lower, middle, and upper safety lines.

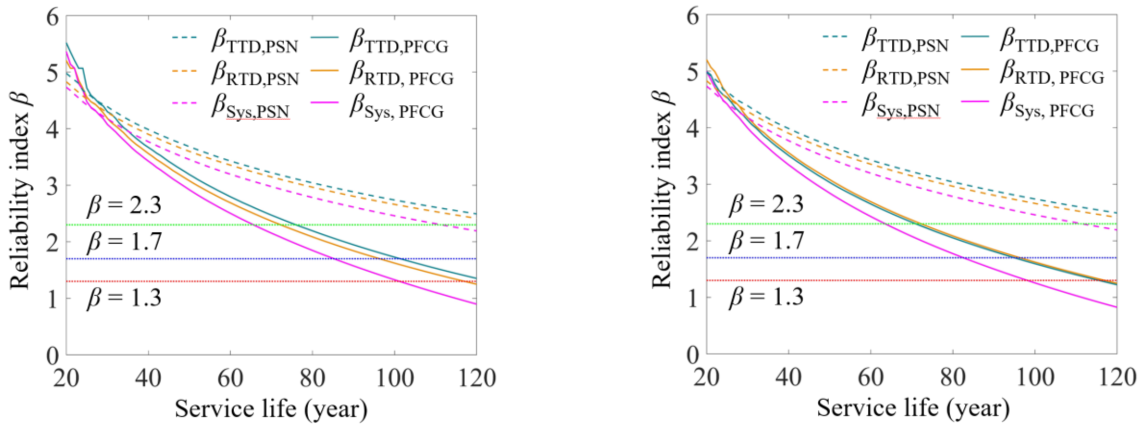


(a) (b)

Fig. 21. Time-variant fatigue reliability: (a) Case I; (b) Case II.

In the case I, the reliability solved by the PFCG is slightly higher than the result by the PSN at the very beginning. With the increase in service life, the PFCG result crosses through the PSN result after about 30 years and decreases at a much higher rate. In terms of the PFCG, the systematic reliability crosses the above three safety lines after about 65, 84, and 100 years, respectively, which stands for the life prediction under the three criteria. On the contrary, the corresponding reliability curve of the PSN decreases below the upper line after roughly 110 years and is well above the other two lines after 120 years. This can be traced back to the nonlinear fatigue damage accumulation in the PFCG model since the SIF increases proportionally with the crack size. As a result, the PSN approach may lead to an overestimated life since the nonlinear damage accumulation is ignored.

The result also shows slightly lower reliability of the RTD in the case I, compared with the TTD cracking. Moreover, the system-level reliability is even lower than that of the RTD, indicating the importance of mixed failure models. For instance, by taking $\beta$ = 1.3 as the bottom line, the fatigue life could be estimated as about 120 years when considering the RTD only. Once the influence of mixed failure models is considered in the system-level reliability, a much shorter life would be resulted as about

100 years. Similar trends can be observed in the result solved under the case II, except that the reliability of the TTD cracking becomes lower than that of the RTD cracking. However, the PSN result stays the same as in the case I since the change in the initial flaw size is not explicitly modelled in the PSN approach.

### 5.3 Crack size evolution

In addition to the fatigue reliability and life prediction, another crucial feature of the PFCG model is the ability to model the variation in crack size explicitly. Thus, the investigation is performed on the time-dependent evolution of the crack size, as shown in Fig. 22. A total of 4 time points is selected, including the 30, 60, 90, and 120 years. For better illustration, the distribution of crack half-length is truncated at a cut-off of 40 mm, above which the probability density drops to an ignorable value.

According to the result, both the mean value and standard deviation of the crack size increase over the service time. As a result, the distribution of crack sizes moves right and transforms from a narrow curve into a flat one. Meanwhile, the distribution density accumulates at the critical crack depth of 16 mm over time, indicating progressive growth in the failure probability. However, the distribution still stays in the almost lognormal form once eliminating the concertation at the critical size. The comparison is made on the size distribution between the toe and root cracks. In general, the mean value of both the crack depth and length are slightly larger in the root crack than in the toe crack. However, an opposite trend could be found in the standard deviation, of which the toe crack has a higher value than the root crack.

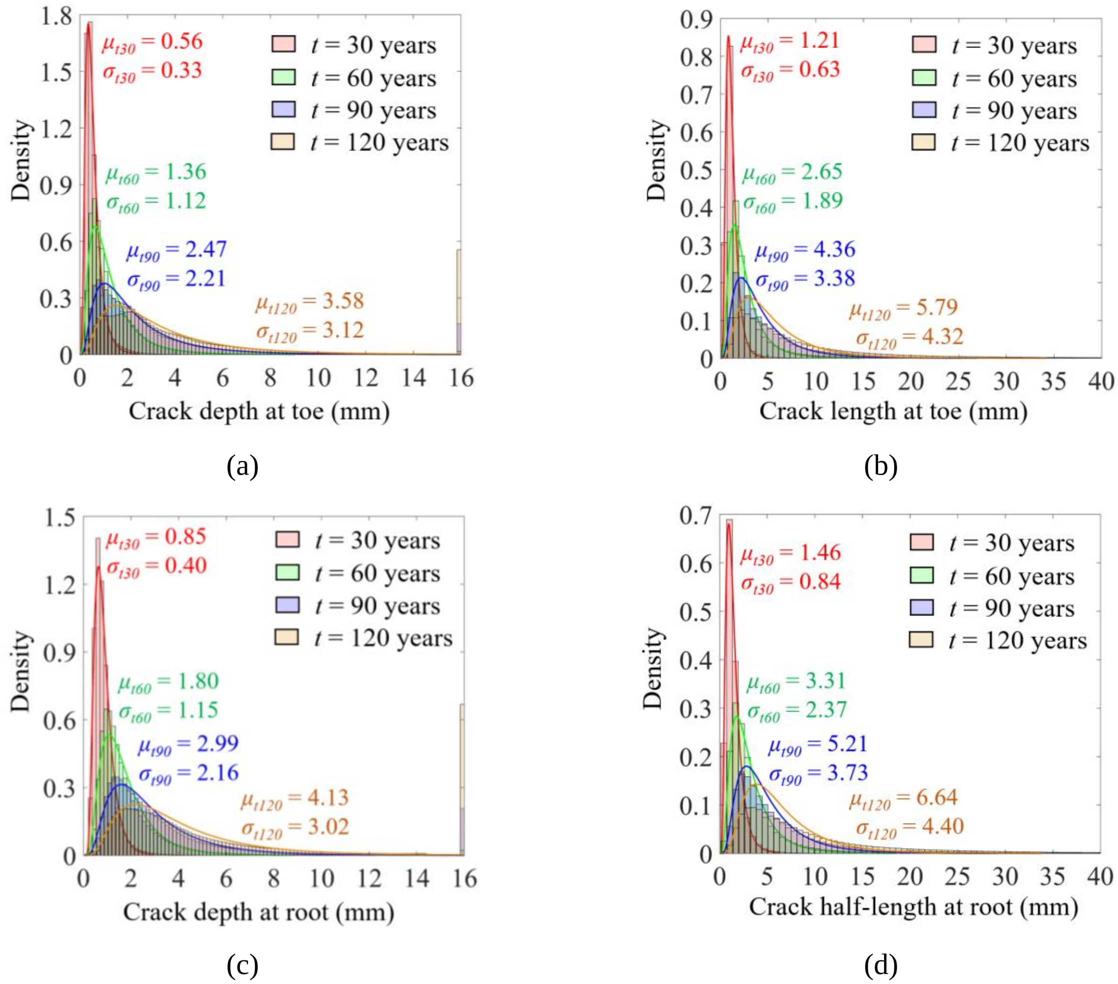


Fig. 22. Crack size distribution at $t$ = 30, 60 and 120 years: (a) crack depth at toe; (b) crack half-length at toe; (c) crack depth at root; (d) crack half-length at root.

In addition, the study also examines the time-dependent variation in the aspect ratio of crack length to depth, as shown by the boxplot in Fig. 23. In both root and toe cracks, the data dispersion decreases from the initial peak value to its trough at 60 years and slowly escalates until 120 years. However, the dispersion at the end of 120 years is still much lower than the initial one. Meanwhile, the aspect ratio distribution also demonstrates a progressive evolution of skewness, i.e., from the initial positive skewness to the normal curve at 40 years and then to the negative skewness at 120 years.

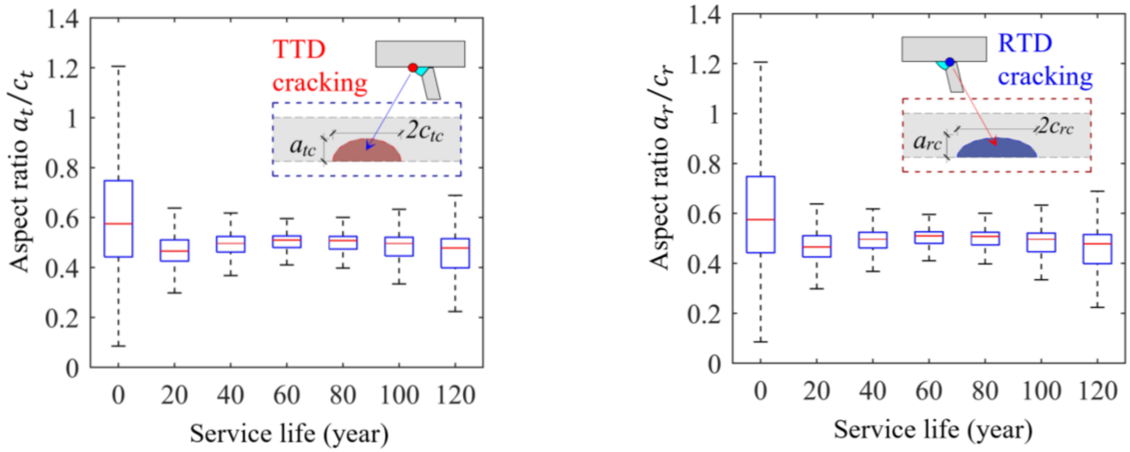


(a) (b)

Fig. 23. Evolution of aspect ratio: (a) Weld toe; (b) Weld root.

## 5.4 Remain fatigue life

Based on the derived crack size distribution, the remain fatigue life of the RD joint could also be estimated, as shown in Fig. 24. According to the result, the distribution moves left with time, indicating the gradual reduction in the remain life. Meanwhile, the probability density gradually accumulates near the value of zero. Accordingly, the distribution changes from the original lognormal shape to the normal form at $t$ = 40 years, and then to the gamma distribution at $t$ = 80 years, and finally to almost the exponential one at the end of $t$ = 120 years. As a result, the failure probability skyrockets even a moderate mean remain life of about 159 years is expected.

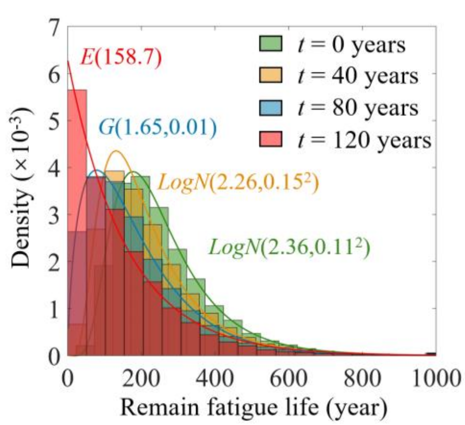


Fig. 24. Distribution of remain fatigue life at $t$ = 0, 40, 80 and 120 years.

## 6. Conclusions

In this study, a probabilistic fatigue crack growth (PFCG) model is established for the rib-to-deck (RD) joint considering the mixed failure models. Based on the observation reported in the literature, two typical failure models are incorporated in the PFCG model, including the toe-to-deck (TTD) cracking and root-to-deck (RTD) cracking. In solving the PFCG model, the Gaussian process regression (GPR) model is used to assist and boost the fracture analysis after well trained. Using the above approach, a series of investigations is carried out on the RD joint respecting the fatigue failure model, fatigue reliability and life prediction, crack size evolution, and remain fatigue life. Above all, the following conclusions are drawn.

(1) Through the application of the GPR to assist in solving the PFCG model, the computational efficiency improves more than 1800 times compared with the pure FE solution. As a result, the PFCG simulation could be implemented with a dedicate balance between accuracy, efficiency, and flexibility.

(2) Besides the TTD and RTD cracking models, the RD joint shows a third cracking model with a very small possibility no more than 2.5%, i.e., the TTD cracking and RTD cracking occurs simultaneously. In the case I when the same initial flaw is assumed, the RD joint is more prone to the RTD cracking (77.7%) than the TTD cracking (20.4%). In the case II when the assumed flaw size is doubled at the weld toe due to the inferior welding quality, the TTD cracking (58.3%) replace the RTD cracking (39.2%) as the dominant one. In both cases, the secondary cracking model shows a notable contribution to fatigue failure in a statistical sense, indicating the importance in considering mixed failure models.

(3) The reliability of the RTD cracking is slightly lower than that of the TTD cracking in the case I, which also indicates the inclination to RTD cracking. More important, the system-level reliability considering mixed failure models is even lower than the RTD cracking. As result, the fatigue life would be overestimated using the dominant cracking model only. For instance, taking $\beta$ = 1.3 as the bottom line, the fatigue life is close to 120 years under the RTD cracking, compared with a shorten life of roughly 100 years in the system-level reliability.

(4) The distribution of crack size shows a steady development in both the mean value and standard deviation, while it stays in almost the lognormal form. As a result, the probability density function gradually moves right and transforms from a narrow curve on the left to a flat one. In terms of the aspect ratio, the dispersity decreases rapidly at the first and then escalates slowly over time. Besides, the distribution of the aspect ratio also shows a progressive evolvement from original positive skewness to the normal form after 40 years, and then to the negative skewness at the end of 120 years.

(5) The remain fatigue life shows a notable transformation in the distribution shape, i.e., from the original lognormal shape to the normal form at 40 years, and to the gamma shape at 80 years, and then to the exponential one at 120 years. As a result, the probability density rapidly enriches in the lower region, which in turn escalates the failure probability quickly even with a notable mean value.

Acknowledgement

The study is supported by the National Natural Science Foundation of China (grant number: 51778536, 52008066).

Conflict of Interest

There is no conflict of interest associated with this publication.

Date Availability Statement

Some or all the data, model or code data employed in this paper are available from the first author upon reasonable request.

References

[1] Kozy, B., Connor, R., Paterson, D., Mertz, D. (2011). Proposed Revisions to AASHTO-LRFD Bridge Design Specifications for Orthotropic Steel Deck Bridges, J. Bridge Eng., 16: 759-767. https://doi.org/10.1061/(ASCE)BE.1943-5592.0000214.

[2] Connor R., Fisher J., Gatti W., et al., Manual for design, construction, and maintenance of orthotropic steel deck bridges, Federal Highway Administration, Washington, DC., US., 2012.

[3] Dooren F., Nagtegaal G., Ashurst D., Gration D., Blanken S., ander & Kunst, Pajc. (2010). Orthotropic Deck Fatigue: Renovation of 8 Bridges in the Netherlands. Structural Faults and Repair-2010: 13th International Conference. https://doi.org/10.13140/RG.2.1.1571.1200.

[4] Kolstein, MH., Fatigue Classification of Welded Joints in Orthotropic Steel Bridge Decks, Gildeprint Drukkerijen B.V., Delft, the Netherlands, 2007.

[5] Zhu, J., Zhang, W., Li, X. (2019). Fatigue Damage Assessment of Orthotropic Steel Deck Using Dynamic Bayesian Networks, Int. J. Fatigue, 118: 44-53. https://doi.org/10.1016/j.ijfatigue.2018.08.037.

[6] Steel Construction Committee of JSCE, Survey and research report by the subcommittee of plate welded joints, JSCE Publications, Tokyo, Japan, 2007. (In Japanese)

[7] Heng, J., Zheng, K., Zhang, Y., Wang, Y. (2018). Enhancing Fatigue Performance of Rib-to-Deck Joints in Orthotropic Steel Decks Using Thickened Edge U-Ribs. In ASCE Struct. Cong. 2018, Reston, VA., US.

[8] Tian, Y., Li, Y., Zhang, D., Dai, Y. (2011). Static and fatigue test research on welded rib-to-deck connections in steel orthotropic steel bridge deck, J. Rail. Sci. Eng., 8(2): 34-39. (In Chinese)

[9] Heng, J., Zheng, K., Gou, C., Zhang, Y., & Bao, Y. (2017). Fatigue performance of rib-to-deck joints in orthotropic steel decks with thickened edge u-ribs, J. BRIDGE ENG., 22(9): 04017059. https://doi.org/10.1061/(asce)be.1943-5592.0001095

[10] Heng, J., Zheng, K., Kaewunruen, S., Zhu, J., Baniotopoulos, C. (2020). Probabilistic fatigue assessment of rib-to-deck joints using thickened edge U-ribs. Steel Compos. Struct., 2, 23-56.

[11] Cheng, B., Ye, X., Cao, X., Mbako, D., Cao, Y. (2017) Experimental study on fatigue failure of rib-to-deck welded connections in orthotropic steel bridge decks, Int. J. Fatigue, 103: 157-167. https://doi.org/10.1016/j.ijfatigue.2017.05.021.

[12] Nagy, W., Wang, B., Culek, B., Bogaert, P., Backer, H. (2017). Development of a fatigue experiment for the stiffener-to-deck plate connection in Orthotropic Steel Decks, Int. J. Steel Struct., 17: 1353-1364. https://doi.org/10.1007/s13296-017-1207-8

[13] Li, M., Suzuki, Y., Hashimoto, K., Sugiura, K. (2018). Experimental Study on Fatigue Resistance of Rib-to-Deck Joint in Orthotropic Steel Bridge Deck. J. Bridge Eng., 23(2): 04017128. https://doi.org/10.1061/(ASCE)BE.1943-5592.0001175.

[14] Ocel J., Cross B., Wright W., Yuan H. Optimization of rib-to-deck welds for steel orthotropic bridge decks, Federal Highway Administration, Washington, DC., US., 2017.

[15] Yamada, K., Ya, S. (2008). Plate bending fatigue tests for root crack of trough rib of orthotropic steel deck, JSCE J. Struct. Eng., 54: 675-684.

[16] Ya, S., Yamada, K., Ishikawa, T. (2010). Fatigue evaluation of rib-to-deck welded joints of orthotropic steel bridge deck. J Bridge Eng., 16(4): 492-499.

[17] Lv, P., Li, D. (2013). Fatigue test study on the rib-to-deck welded joint in orthotropic steel decks, J. Zhengzhou Univ. (Eng. Sci.), 34(2): 89-93. (In Chinese)

[18] Fu, Z., Ji, B., Zhang, C., Wang, Q. (2017). Fatigue performance of roof and U-rib weld of orthotropic steel bridge deck with different penetration rates, J Bridge Eng., 22(6): 04017016.

[19] Sim, H., Uang, C., Sikorsky, C. (2009). Effects of Fabrication Procedures on Fatigue Resistance of Welded Joints in Steel Orthotropic Decks, Journal of Bridge Engineering, J. Bridge Eng., 14(5): 366-373. https://doi.org/10.1061/(ASCE)1084-0702(2009)14:5(366).

[20] Kainuma, S., Yang, M., Jeong, Y., Inokuchi, S., Kawabata, A., Uchida, D. (2016). Experiment on fatigue behavior of rib-to-deck weld root in orthotropic steel decks, J. Constr. Steel Res., 119: 113-122. https://doi.org/10.1016/j.jcsr.2015.11.014.

[21] Wang, C., Zhai, M., Tang, Y., Chen, W., Qu, T. (2017). Numerical Fracture Mechanical Simulation of Fatigue Crack Coupled Propagation Mechanism for Steel Bridge Deck. China J. Highway & Transport, 30(3): 82-95. (In Chinese)

[22] Li, J., Zhang, Q., Bao, Y., Zhu, J., Chen, L., Bu, Y. (2019). An equivalent structural stress-based fatigue evaluation framework for rib- to-deck welded joints in orthotropic steel deck. Eng. Struct. https://doi.org/196. 10.1016/j.engstruct.2019.109304.

[23] Luo, P., Zhang, Q., Bao, Y., Zhou, A. (2018). Fatigue evaluation of rib-to-deck welded joint using averaged strain energy density method, Eng. Struct., 177: 682-694. https://doi.org/10.1016/j.engstruct.2018.09.090.

[24] European committee for standardization (CEN), EN 1993: Eurocode 3 - design of steel structures, CEN, Brussels, Belgium, 2005.

[25] Ministry of communications of the People's Republic of China. Specifications for design of highway steel bridges (GB/T D64-2015), CCPress, Beijing, China, 2015. (in Chinese).

[26] AASHTO, AASHTO LRFD bridge design specifications, 9th edition. Washington, DC., US., 2020.

[27] Shen, C. (1994). The statistical analysis of fatigue data, PhD Thesis, University of Arizona, Tucson.

[28] Anderson, TL., Fracture Mechanics: Fundamentals and Applications (Fourth Edition), CRC press, Baca Raton, FL, US., 2017.

[29] Berg, N., Xin, H., Veljkovic, M. (2020). Effects of residual stresses on fatigue crack propagation of an orthotropic steel bridge deck, Mater. Design, 198(2021), 109294 https://doi.org/10.1016/j.matdes.2020.109294.

[30] Biondini, F., Frangopol, D. (2016). Life-Cycle Performance of Deteriorating Structural Systems under Uncertainty: Review. J. Struct. Eng., 142: F4016001. https://doi.org/10.1061/(ASCE)ST.1943-541X.0001544.

[31] Hobbacher, A. (2016), Recommendations for Fatigue Design of Welded Joints and Components, Springer, Basel, Switzerland.

[32] European committee for standardization, EN 1991: Eurocode 1 - Actions on structures - part 2: traffic loads on bridges, CEN, Brussels, Belgium, 2003.

[33] Kwon, K., Frangopol, D. (2010). Bridge fatigue reliability assessment using probability density functions of equivalent stress range based on field monitoring data, Int. J. Fatigue, 32: 1221-1232. https://doi.org/10.1016/j.ijfatigue.2010.01.002.

[34] Heng, J., Zheng, K., Kaewunruen, S., Baniotopoulos C. (2019). Stochastic Traffic-Based Fatigue Life Assessment of Rib-to-Deck Welding Joints in Orthotropic Steel Decks with Thickened Edge U-Ribs, Appl. Sci., 9(13): 2582. https://doi.org/10.3390/app9132582

[35] Zhu, J., Zhang, W. (2018). Probabilistic fatigue damage assessment of coastal slender bridges under coupled dynamic loads, Eng. Struct., 166: 274-285. https://doi.org/10.1016/j.engstruct.2018.03.073.

[36] Liu, Y., Mahadevan, S. (2009). Probabilistic fatigue life prediction using an equivalent initial flaw size distribution, Int. J. Fatigue, 31: 476-487. https://doi.org/10.1016/j.ijfatigue.2008.06.005.

[37] Righiniotis, TD., Chryssanthopoulos, MK. (2003). Probabilistic fatigue analysis under constant amplitude loading, J. Constr. Steel Res., 59(7): 867-886.

[38] Guo, T., Frangopol, D., & Chen, Y. (2012). Fatigue reliability assessment of steel bridge details integrating weigh-in-motion data and probabilistic finite element analysis, COMPUT. STRUCT., 112-113(4): 245-257. https://doi.org/10.1016/j.compstruc.2012.09.002

[39] Heng, J., Zheng, K., Kaewunruen, S., Zhu, J., & Baniotopoulos, C. (2019). Dynamic Bayesian network-based system-level evaluation on fatigue reliability of orthotropic steel decks. ENG. FAIL. ANAL., 105, 1212-1228. https://doi.org/10.1016/j.engfailanal.2019.06.092

[40] Maljaars, J., Vrouwenvelder, A. (2014). Probabilistic fatigue life updating accounting for inspections of multiple critical locations, Int. J. Fatigue, 68: 24-37.

[41] Maljaars, J., Bonet, E., Pijpers, R. (2018). Fatigue resistance of the deck plate in steel orthotropic deck structures. Eng. Fract. Mech. 201: 214-228. https://doi.org/10.1016/j.engfracmech.2018.06.014.

[42] Wang, B., Zhou, X., Backer, H., Chen, A., Schmidt, F. (2017). Macro-crack initiation life for orthotropic steel decks considering weld heterogeneity and random traffic loading, Struct. Infrastruct. Eng., 13(12): 1639-1652. https://doi.org/10.1080/15732479.2017.1315733

[43] Gupta, RS., Xin, H., & Veljkovic, M. (2019). Fatigue crack propagation simulation of orthotropic bridge deck based on extended finite element method. Procedia Structural Integrity, 22: 283-290. https://doi.org/10.1016/j.prostr.2020.01.036

[44] Kountouris, IS., Baker, MJ. (1989). Defect assessment: analysis of the dimensions of defects detected by ultrasonic inspection in an offshore structure, CESLIC Report OR8. Imperial College of Science and Technology, London, UK.

[45] British Standards Institution (BSI). BS 7910:2015 Guide to methods for assessing the acceptability of flaws in metallic structures, BSI Standards Limited, London, UK, 2015.

[46] Schork, B., Kucharczyk, P., Madia, M., Zerbst, U., Hensel, J. & Bernhard, J. & Tchuindjang, Didi Deflor & Kaffenberger, Matthias & Oechsner, M.. (2017). The effect of the local and global weld geometry as well as material defects on crack initiation and fatigue strength. Eng. Fract. Mech., 198: 103-122. https://doi.org/10.1016/j.engfracmech.2017.07.001.

[47] Zerbst, U., Ainsworth, RA., Beier, HTh., Pisarski, H., Zhang, Z., Nikbin, K., & Nitschke-Pagel, T., Muenstermann, S., Kucharczyk, P., Klingbeil, D. (2014). Review on fracture and crack propagation in weldments - A fracture mechanics perspective, Eng. Fract. Mech., 132: 200-276. https://doi.org/10.1016/j.engfracmech.2014.05.012.

[48] Bell, R., Vosikovsky, O., Bain, S. (1989). The Significance of Weld Toe Untercuts in the Fatigue of Steel Plate T-Joints, Int. J. Fatigue, 11(1): 3-11. https://doi.org/10.1016/0142-1123(89)90041-8.

[49] Guo, T., Liu, Z., Zhu, JS. (2015). Fatigue reliability assessment of orthotropic steel bridge decks based on probabilistic multi-scale finite element analysis, Adv. Steel Constr., 11: 334-346. https://doi.org/10.18057/IJASC.2015.11.3.7.

[50] Lu, N., Liu, Y., Deng, Y. (2018). Fatigue Reliability Evaluation of Orthotropic Steel Bridge Decks Based on Site-Specific Weigh-in-Motion Measurements, Int. J. Steel Struct., 19: 181-192. https://doi.org/10.1007/s13296-018-0109-8.

[51] ANSYS. Engineering Simulation and 3D Design Software; ANSYS Inc., Canonsburg, US. http://www.ansys.com/

[52] ANSYS (2020). Mechanical APDL Documentation, ANSYS Inc., Canonsburg, PA, US.

[53] Amzallag, C., Gerey, J. P., Robert, J. L., Bahuaud, J. (1994). Standardization of the rainflow counting method for fatigue analysis, Int. J. Fatigue, 16(4): 287-293. https://doi.org/10.1016/0142-1123(94)90343-3

[54] Rasmussen, CE., Nickisch, H. (2010). Gaussian processes for machine learning (GPML) toolbox. The Journal of Machine Learning Research, 11, 3011-3015.

[55] Kim, NH., An, D., Choi, JH. Prognostics and health management of engineering systems. Springer International Publishing, Switzerland, 2017. https://doi.org/10.1007/978-3-319-44742-1

[56] Intel. Central processing units; Intel Inc., Santa Clara, CA., US. http://www.intel.com/

[57] Devore JL., Probability and statistics for engineering and the sciences, Cengage learning, Boston, 2011. https://doi.org/10.2307/2532427

[58] Imam, B., Chryssanthopoulos, M. (2010). A review of metallic bridge failure statistics. In Proceedings of the Fifth International IABMAS Conference, Philadelphia, US.

[59] JCSS. probabilistic model code, part 1: basis of design, JCCS, Aalborg, 2000.